Nanoscale mechanical actuation and near-field read-out of photonic crystal molecules

Nanoscale mechanical actuation and near-field read-out of photonic crystal molecules

M. Petruzzella,[1,*] F. La China,[2,3] F. Intonti,[2,3] N. Caselli,[2,3] M. De Pas,[2] F. W. M. van Otten,[1] M. Gurioli,[2,3] and A. Fiore[1]

[1]*COBRA Research Institute, Eindhoven University of Technology, P.O. Box 513, NL-5600MB Eindhoven, The Netherlands*

[2]*European Laboratory for Non-Linear Spectroscopy, 50019 Sesto Fiorentino (FI), Italy*

[3]*Department of Physics and Astronomy, University of Florence, Via G. Sansone 1, 50019 Sesto Fiorentino (FI), Italy*

(Received 26 May 2016; revised manuscript received 9 August 2016; published 8 September 2016)

We employed the contact forces induced by a near-field tip to tune and probe the optical resonances of a mechanically compliant photonic crystal molecule. Here, the pressure induced by the near-field tip is exploited to control the spectral proprieties of the coupled cavities in an ultrawide spectral range, demonstrating a reversible mode shift of 37.5 nm. Besides, by monitoring the coupling strength variation due to the vertical nanodeformation of the dielectric structure, distinct tip-sample interaction regimes have been unambiguously reconstructed with a nano-Newton sensitivity. These results demonstrate an optical method for mapping mechanical forces at the nanoscale with a lateral spatial resolution below 100 nm.

DOI: 10.1103/PhysRevB.94.115413

I. INTRODUCTION

The inherent coupling between motion and light is at the core of a wide research area ranging from gravitational waves detection [1] to cavity optomechanics [2]. From a fundamental perspective, the interaction of mechanical oscillators with photons promises to bring quantum phenomena, such as superposition and entanglement, into the macroscopic realm [3]. On the application side, engineering such coupling may boost the sensitivity of displacement measurements, enabling novel integrated accelerometers [4] and high-precision mass sensors [5].

Among the numerous nanophotonic platforms investigated during the past decade, photonic crystal cavities (PhCCs) represent an excellent toolbox for metrology and sensing applications, due to their ultranarrow resonances localized in diffraction-limited dielectric volumes [6]. Optomechanical effects on mechanically compliant PhCC systems, such as dynamical back action, have been extensively studied [7,8], while several proposals have been advanced in the context of force sensing, including multichannel movable PhC wave guides [9,10] and flexible PhCC cantilevers [11].

A different approach, which relies on a dual-layer PhC membranes, was theoretically presented in Ref. [12] and further elaborated in Refs. [13] and [14]. This system has been experimentally investigated in the context of optomechanics [15] and its electromechanical actuation has been demonstrated [16] and exploited for cavity quantum electrodynamics experiments [17,18].

In this paper, we experimentally study the effect of local forces exerted by a near-field probe on a mechanically reconfigurable bilayer photonic crystal resonator. We employ near-field methods not only to monitor the local density of optical states in real time, but also to induce a mechanical and reversible local deformation of the structure. We provide a robust demonstration of this pull-in-free actuation scheme, achieving a record spectral tuning of 37.5 nm per mode. Then, viceversa, we exploit our device as force nanosensor to unambiguously identify distinct contact regimes characterized by either repulsive or attractive potential.

*m.petruzzella@tue.nl

The photonic molecule under study [see inset of Fig. 1(a)] consists of two nominally identical photonic crystal cavities realized on two parallel membranes, separated by a distance d along the growth direction. The physical concept underpinning the operation of the device can be explained in light of the temporal coupled mode theory (TCMT) [19]. Indeed, when d is small enough that the out-of-plane evanescent field of one slab penetrates into the other, the degenerate original modes of the two membranes hybridize, originating a pair of super-modes. The latter are delocalized over the two membranes and inherit the in-plane symmetry of the original uncoupled modes. In analogy with the bonding and antibonding electronic wave function of homoatomic molecules, the original photonic states split in symmetric (S) and antisymmetric (AS) modes [20]. Their energy separation is $\Omega_{\mathrm{s,\,as}} = \sqrt{\delta^2 + 4g^2}$, where δ accounts for a possible energy mismatch between the uncoupled modes and g represents the coupling constant given by the spatial overlap of the two uncoupled modes weighted by the dielectric constant perturbation [21]. The coupling of the optical spectrum to the mechanical degree of freedom is realized by fabricating the upper crystal on a suspended microbridge [Fig. 1(a)]. In this way, a perturbation (δd) of the membrane position due to an external vertical force (δF) is directly transduced into the optical domain as a change in the splitting energy ($\delta\Omega$) of the coupled modes via the change in the coupling constant (δg).

Specifically, the selected bridge geometry is composed of a rectangular photonic crystal area connected to a supporting frame by four external microarms ($2\times2\,\mu\mathrm{m}^2$). The area of the bridge ($14\times8\,\mu\mathrm{m}^2$) ensures a sufficient in-plane confinement around the cavity defect. Additional external trenches are patterned close to the supporting arms to release any internal stress accumulated during the fabrication process and to avoid buckling of the structure [22].

In order to relate the effect of a vertical local force to the deformation of the bridge we solve the static elasticity equation employing a finite element method (FEM) algorithm [Fig. 1(b)]. In particular, we model the local force exerted by the near-field probe as a load (F) uniformly distributed over a circle of radius $R = 100\,\mathrm{nm}$ located at the center of the membrane. The deformation along the vertical direction, here encoded in a color scale, manifests a parabolic dependence

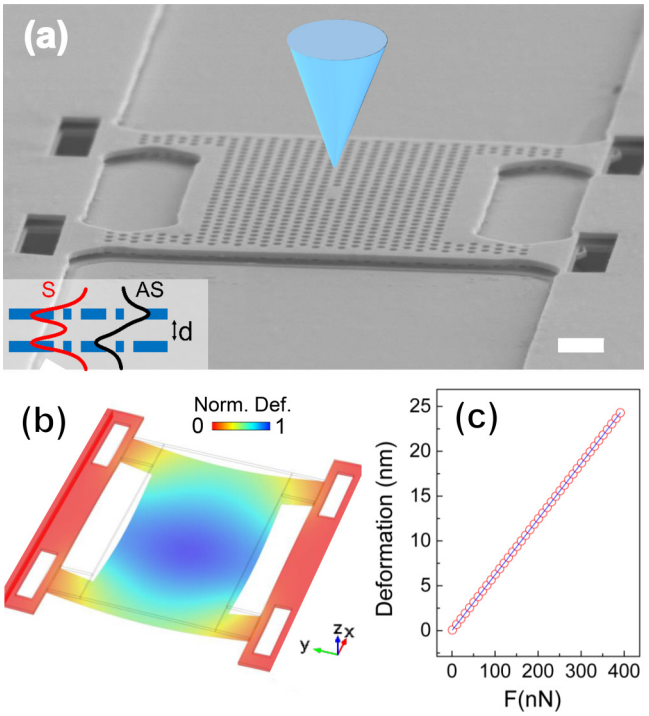

FIG. 1. (a) Scanning electron micrograph showing the upper free-standing PhC microbridge. The scale bar corresponds to 1 μm. (b) FEM simulation of the vertical deformation of the structure caused by a localized force applied at the center of the bridge. (c) Calculated linear dependence of the maximum displacement on the applied force.

on the x coordinate due to the boundary conditions of this geometry. The maximum deformation is obtained at the center of the membrane where the cavity is located. This displacement is linearly dependent on the applied force [Fig. 1(c)] through an effective spring constant $k = 16\,\mathrm{N/m}$.

II. METHODS

The fabrication of the device has been previously reported and comprises several steps of optical and electron beam lithography followed by dry and selective wet etching processes, for the release of the membranes [23]. The sample consists of two free-standing Gallium Arsenide membranes that are both nominally 170 nm thick. The photonic crystal pattern, composed of a triangular array of holes (lattice constant $a = 380$ nm, filling ratio $f = 0.32$, holes radius $r = 113$ nm) is etched through both membranes [Fig. 1(a) inset]. A point-defect cavity is realized by removing three inline holes from the lattice (L3). In the middle of the top slab a layer of high-density self-assembled InAs quantum dots is grown. The ground-state emission of these internal sources is centered around 1305 nm at room temperature and the QD photoluminescence spans over more than 100 nm, including the excited states and the overall inhomogeneous broadening.

A commercial scanning near-field microscope (Twinsnom, OMICRON) is operated in the illumination and collection geometry. In the following experiments a pure dielectric tip, which is a glass tapered optical fiber obtained by chemical etching [24], is exploited both as a near-field probe to collect the photoluminescence spectrum and, simultaneously, to apply a controlled local nN force. To this end, a 780-nm diode laser is coupled to an optical fiber that terminates in the near-field tip in order to excite the QD photoluminescence. Then, the emitted light is collected from the same fiber and separated from the excitation radiation by a dichroic beam splitter, finally dispersed by a spectrometer and detected by a liquid-nitrogen-cooled InGaAs array. The control of the tip-surface separation is realized through the shear-force technique. The probe is attached to a bimorph piezo set to oscillate laterally with a constant amplitude of a few Å and the oscillation phase shift, which occurs in presence of contact forces when the tip-sample distance is below 10 nm, is maintained constant by a piezoelectric feedback loop. The sample is mounted on a XYZ piezoelectric scan stage, which enables the X-Y nm and the Z sub-nm control over the sample-tip position.

III. RESULTS AND DISCUSSION

Figure 2 shows the spectral evolution of the antisymmetric (left panel) and symmetric (right panel) modes when the z position of fiber apex is varied. In this experiment, the tip is positioned above the cavity and then moved downward until it reaches the position z_F, where the spring force of the upper membrane is large enough that the tip-membrane spacing reaches the value fixed by the phase set point of the feedback loop. Then, the tip is moved upward, from the minimum $z_F = -30\,\mathrm{nm}$ to the maximum $z_{UP} = 17\,\mathrm{nm}$ with a constant speed of 7 nm/s (with the feedback loop turned off), while the spectra are continuously acquired at a frequency of 10 Hz. The origin of the z axis is defined as the point where the splitting between the coupled modes is minimum. In this way, the intensity maps shown in Fig. 2 are reconstructed. From a comparison with finite-element method simulations, these modes have been identified as the fundamental symmetric (Y_S^1 right panel) and antisymmetric (Y_{AS}^1, left panel) mode of the investigated photonic molecule, which exhibit the

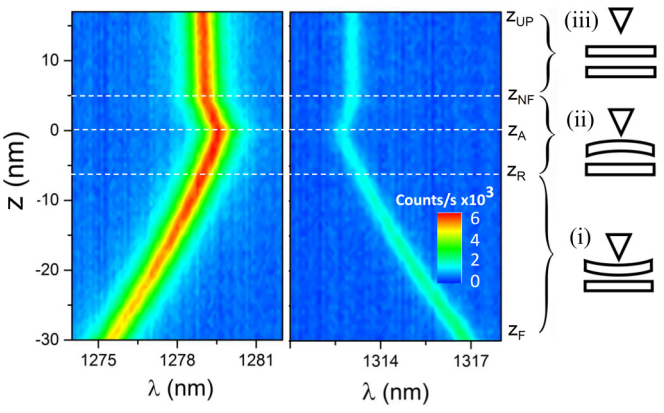

FIG. 2. Color-encoded photoluminescence spectra of the antisymmetric (left panel) and symmetric (right panel) mode acquired while varying the z position of the tip from $z = z_F$ to above the sample ($z > z_{NF}$), where no external force is applied and the membranes are at the unperturbed distance. The tip vertical position is measured with 0.7-nm resolution, while the $z = 0$ origin is set at the minimum splitting.

principal polarization perpendicular to the defect line. Based on the energy splitting of the coupled modes, we can identify three interaction regimes accordingly to the different vertical positions z of the tip: (i) $z < z_R$, tip pushing membrane; (ii) $z_R < z < z_{NF}$, tip pulling membrane; (iii) $z > z_{NF}$, no force.

From $z_{NF} = 5$ nm to $z_{UP} = 17$ nm [region (iii)], the splitting energy remains practically unperturbed ($\Omega_{NF} = 25.0$ meV). Therefore, the contact force exerted by the tip is negligible for z larger than z_{NF} and the value of Ω_{NF} corresponds to the splitting of the modes when the two membranes are parallel at their initial distance.

In region (i), which extends from $z_F = -30$ nm to $z_R = -7$ nm, the two modes shift along opposite directions while the splitting decreases. This feature corresponds to an upward displacement of the (top) membrane due to the release of the tip pressure. In this region the value of the intermembrane distance is a one-to-one function of the tip position $d(z) = \overline{d} - |z_R - z|$, where $\overline{d}$ is the initial intermembrane distance. Notably, from $z_R = -7$ nm to $z_A = 0$ [region (ii)], the splitting further decreases to $\Omega_A = 24.5$ meV, below the value of Ω_{NF}, indicating that the intermembrane gap is larger compared to the case where no force is applied. This effect arises from an attractive force between the tip and the membrane, characterized by a very short range (few nm), possibly originated by the Van der Walls interaction between the tip and the membrane and/or by the surface tension due to the presence of a water meniscus on the surface of the wafer [25].

Finally, in region (ii) from $z_A = 0$ to $z_{NF} = 5$ nm, the splitting energy increases to Ω_{NF}, corresponding to a decrease of the intermembrane gap to its equilibrium value, caused by the removal of the attractive force applied by the tip.

Noteworthy, the ability of discriminating the sign of the contact force at such small distances with high spatial resolution (see below), represents a key advantage of this system.

In order to give a quantitative estimation of the forces and the physical variables that come into play, in what follows, we focus on the actuation regime ($z \leqslant 0$).

Figure 3(a) reports a record tuning acquired when the fiber tip is operated in the repulsive mode and exerts a compressive force on the device. An offset between the different spectra is introduced for clarity. During this experiment, differently from the one in Fig. 2, the sample is moved in steps and its movement triggers the acquisition of the photoluminescence spectrum. The total wavelength tuning of Y_S^1 for the z range investigated in this experiment is 37.5 nm, which is more than three times larger than the record tuning achieved by using the electromechanical forces on similar devices [17]. Indeed a clear advantage of this technique compared to the electrostatic tuning [26,27] rests with the absence of a pull-in limit (1/3 of the initial gap), which is exploited in the following to validate the theoretical predictions for a wide range of coupling values. Additional modes enter the experimental spectral window for $z = -70$ nm and correspond to high-order symmetric modes. A crossing with the Y_{AS}^1 is observed, denoting a very small coupling (if any) between these modes.

A monotonic decrease in the quality factor (Q) of both Y_S^1 and Y_{AS}^1 is observed during the tuning experiment [Fig. 3(b), upper panel]. This trend is consistent with the behavior predicted by three-dimensional FEM simulations

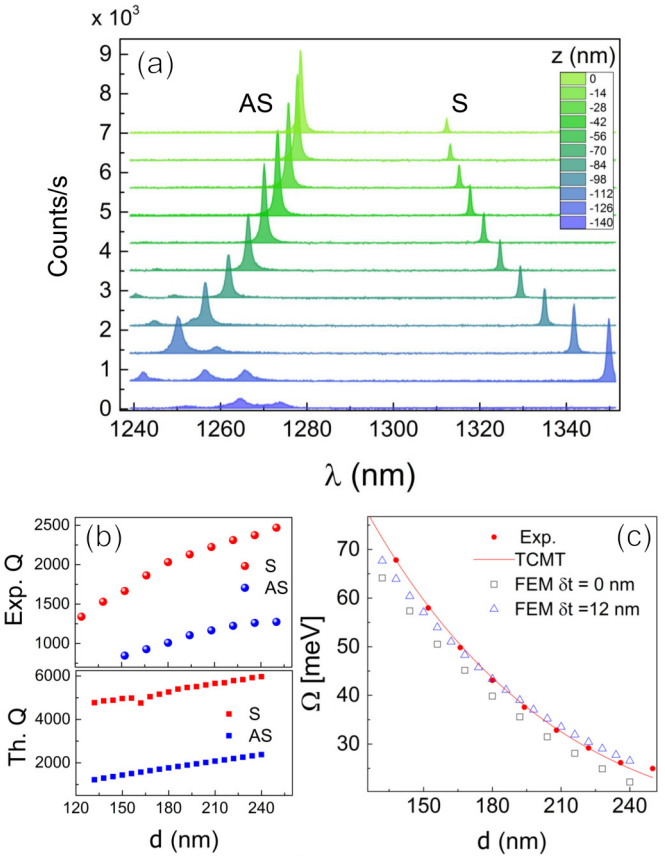

FIG. 3. Actuation of the photonic crystal molecule due to the mechanical contact force induced by the tip. (a) The wavelength of the symmetric (antisymmetric) fundamental mode decreases (increases) when the tip is moved upwards. Experimental (b, top panel) and simulated (b, bottom panel) quality factors as a function of the gap d. (c) Experimental (red dots) and analytical fit (solid line) of the splitting energy (Ω) of the photonic crystal molecule. The simulated splitting with zero (black squared) and 12-nm (blue triangles) thickness asymmetry (δt) is shown for comparison.

[Fig. 3(b), bottom panel], assuming the nominal initial distance of $\overline{d} = 250$ nm and neglecting the presence of the tip. The increase in losses when reducing the slab distance is attributed to the complex interplay between interference effects [28] and the change in fraction of the k-vector components lying inside the light cone for the two modes [23]. Still, the experimental values of Q are smaller than the theoretical ones. This discrepancy is attributed to fabrication deviations, which introduce a degree of randomness in the position and radii of the pores, and lower the experimental Q.

Since we have direct access to the value of the intermembrane distance, we can quantitatively compare the experimental splitting with the one predicted by FEM simulations. Figure 3(c) shows that the measured splitting energy (red circles) is significantly larger than the simulated values (black squares). This discrepancy can be related to an asymmetry in the membrane thickness (δt), arising from the imperfect selectivity of the etching processes, which can reduce the final thickness of the upper membrane by few tens of nanometers [23]. As a consequence, the original uncoupled modes are

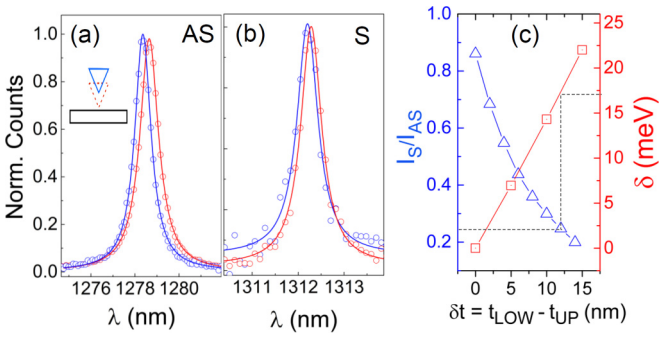

FIG. 4. Red-shift induced by the dielectric perturbation on the AS (a) and S (b) mode when the tip is brought from $z > 100$ nm to contact. (c) Simulated ratio between the field squared of the S and AS mode at $z = 0$ (c, blue triangles) and detuning δ (c, red squares) as a function of the thickness difference between the lower and upper membrane ($t_{\mathrm{LOW}} = 170$ nm).

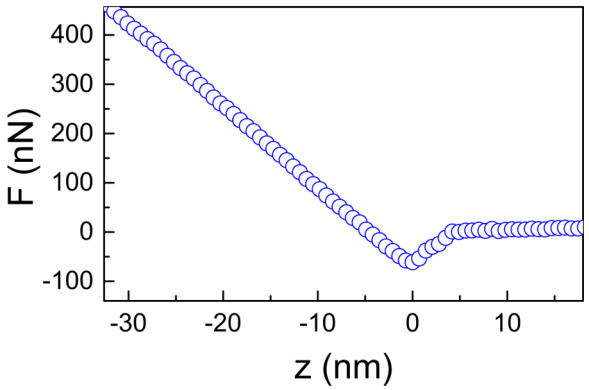

FIG. 5. Force applied by the tip, derived assuming a spring constant $k = 16\,\mathrm{N/m}$. The positive (negative) values corresponds to a repulsive (attractive) regime.

characterized by a nonnegligible energy mismatch δ, which increases the actual splitting energy.

In order to validate this hypothesis, we examine other possible signatures of the thickness difference between the membranes in our spectral data. In particular, we can extrapolate δ from the different frequency perturbations induced by the presence of the dielectric tip in the near-field of the S and AS mode [29,30]. Indeed, when the tip is brought from well above the cavity ($z = 112$ nm), where the tip perturbation can be considered negligible [31], to the contact z_{NF} both modes experience a red-shift, but with a magnitude proportional to their electric field intensity $\mathrm{I_N}$ (N = S, AS) at the tip position (i.e., on the upper membrane). Figure 4 shows that the tip-induced shift is larger for the AS mode (0.08 and 0.28 nm obtained from the Lorentzian fit for the S and AS mode, respectively). Besides, the tip introduces an additional loss channel, which results in a small decrease (13%) of the Q of the AS mode, while this reduction is below the fitting error for the S mode. By averaging over an area of 200×250 nm^2 (20 z scans), centered around the first lobe of the in-plane mode distribution, we derive an experimental energy shift of $\delta E_{\mathrm{S}} = (50 \pm 10)\ \mu$eV and $\delta E_{\mathrm{AS}} = (210 \pm 30)\ \mu$eV. Here the error is calculated from the standard deviation of the shift among the different scans. The ratio of the mode intensity just above the top membrane can therefore be calculated as $\frac{\mathrm{I_S}}{\mathrm{I_{AS}}} = \frac{\delta E_{\mathrm{S}}}{\delta E_{\mathrm{AS}}} = 0.24 \pm 0.08$. The relative intensities of the S and AS modes on the top membrane sensitively depend on the membrane thickness asymmetry, since the S (AS) mode tends to localize in the thicker (thinner) membrane. Figure 4(c) reports the simulated intensity ratio between the two modes and the calculated detuning as a function of the thickness difference between the lower and upper membrane ($t_{\mathrm{LOW}} - t_{\mathrm{UP}}$). From this data, we can estimate a thickness asymmetry of $\delta t \sim 12$ nm, which produces an energy detuning $\delta \sim 17$ meV.

A further confirmation of this asymmetry can be found in the opposite behavior of the integrated intensity of the S and AS modes as a function of the intermembrane distance [Fig. 3(a)]. Indeed, when d is reduced the collected PL intensity of Y^1_{S} (Y^1_{AS}) significantly increases (decreases). This effect is not caused by the change in Q factor through the Purcell-enhanced spontaneous emission, since the latter shows the same trend for the two modes. Rather, as mentioned above, the field tends to localize in the thicker membrane, when the energy difference between the uncoupled modes is significant with respect to the coupling g. As the QDs are positioned in the top membrane, this produces a stronger PL intensity in the AS mode at large membrane distance, as observed in Fig. 3(a). The difference in PL intensities is reduced for smaller distances as the coupling increases, leading to a more equal distribution of the modes over the two membrane.

By introducing the thickness asymmetry $\delta t = 12$ nm derived from the near-field shifts of Fig. 4, a better overlap of the experimental and simulated tuning curve is obtained [Fig. 3(c), triangles].

Intriguingly, from these data we can extrapolate the value of the coupling constant as a function of the gap expected from the TCMT. This can be expressed analytically as $g = g_0 e^{-d/d_0}$, where g_0 represents the spatial integral of the in-plane profiles weighted on the dielectric constant of the material, and d_0 provides the spatial decay constant of the evanescent field. From the least square fit to the experimental data [continued line in Fig. 3(c)], we obtain $g_0 = (172 \pm 5)$ meV and $d_0 = (83 \pm 2)$ nm. The values of δ, g_0, and d_0 allow calculating the intermediate distance d for each tip position z, through the relation $\Omega = \sqrt{\delta^2 + 4(g_0 e^{-d/d_0})^2}$. This, together with the calculated spring constant, is used to derive the value of the force applied by the tip in the different regimes described in Fig. 2. The resulting plot [Fig. 5(b)] in the region around $z = 0$ is similar to the typical force-distance curve obtained in a SNOM as measured by standard atomic force microscopy (AFM) [32]. The high sensitivity of the system enables to identify the adhesion part of the interaction ($F < 0$), and the maximum value of the attractive force is obtained as $F \sim -60$ nN at $z = 0$. The force resolution of the present measurement is limited by the signal to noise ratio of the SNOM PL. Employing a laser scattering configuration [33] will allow us to investigate the tip-sample mechanical interaction with a resolution possibly in the sub-pN range.

Finally, we compare the topography derived by the bimorph piezo feedback signal [Fig. 6(a)] and the topography reconstructed optically from the wavelength shift of the fundamental AS mode at the feedback loop set point (z_{F})

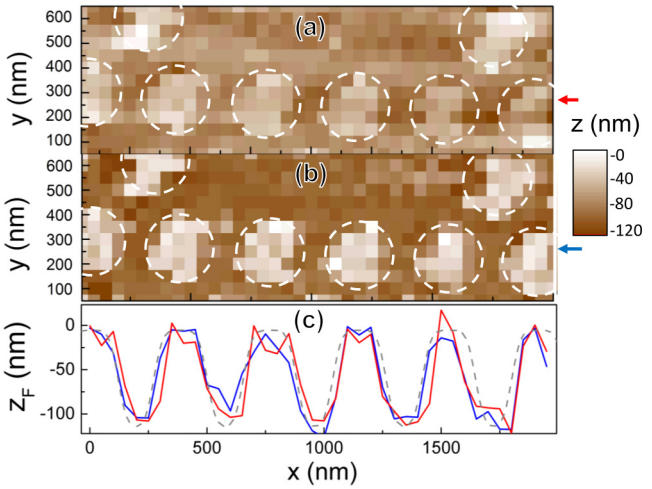

FIG. 6. Topography map readout from the feedback loop (a) and optical topography reconstructed from the wavelength shift of the fundamental AS mode (b). (c) Two line scans taken at the arrow positions (red for the topography obtained from the optical shift, blue for topography derived from the feedback loop) compared with the nominal topography convoluted with a Gaussian point spread function with FWHM = 70 nm.

acquired at several (x, y) positions [Fig. 6(b)]. Here the scan consists of 40×20 pixels ($2\,\mu\text{m} \times 1\,\mu\text{m}$) centered around the cavity defect. The two topography maps show an excellent agreement, confirming our interpretation of the experiment. Large variations of the tip and membrane vertical positions are observed along the scan, showing that the actuation range depends on the in-plane position of the tip. In particular, if the tip is located above a pore (white areas) the actuation is less effective as compared to the configuration where the tip is positioned on the semiconductor region. This results in *inverted* topography maps. The cause of this effect can be ascribed to the presence of lateral forces arising inside the pore volume, which increases the damping in the lateral oscillations of the tip compared to the bulk regions. Since the feedback loop controls the vertical position of the tip by maintaining its oscillation phase constant while scanning along the lateral direction, the effective force applied by the tip is larger in the bulk area resulting in a larger vertical displacement of the membrane and in a dip in the topography. This feature illustrates the peculiar local character of this actuation experiment. Figure 6 shows a line scan extracted from the 2D topographies. The gray dashed curve corresponds to the best fit obtained through the convolution of a step function with a gaussian point function, characterized by a full-width at half maximum FWHM = 70 nm. The latter represents an estimate of the spatial resolution of this tuning scheme.

IV. CONCLUSIONS

In conclusion, we studied the optomechanical coupling of a near-field probe and a nanomechanical resonator composed of a reconfigurable photonic crystal molecule. We demonstrated that this interaction can be used to implement a local reversible actuation scheme, achieving record energy tuning on PhC cavity modes. The accurate modeling of the optical proprieties of the device, combined with the near-field read-out of the field, highlights the role of the detuning in the emitted luminescence signal. Additionally, the splitting of the coupled mode provides a real-time monitor parameter on the dynamics of the contact forces. The device investigated in this work can represent a fundamental building block for integrated sensing applications, and open the way to nanoscale force microscopy integrated on a semiconductor platform.

ACKNOWLEDGMENTS

The authors acknowledge fruitful discussions with R. W. van der Heijden, Z. Zobenica, M. Cotrufo, F. M. Pagliano, E. J. Geluk, and E. B. Smalbrugge. N.C., F.L.C., M.G., and F.I. declare to be supported by the FET Project No. FP7 618025 CARTOON and the project LASERLAB-EUROPE (284464, EC FP7). M.P. and A.F. declare to be supported by the project LASERLAB-EUROPE (No. 284464, EC FP7) and by the Dutch Technology Foundation Stichting voor de Technische Wetenschappen (STW), Applied Science Division of NWO, the Technology Program of the Ministry of Economic Affairs under Project No. 10380.

[1] B. P. Abbott, R. Abbott, T. D. Abbott, M. R. Abernathy, F. Acernese, K. Ackley, C. Adams, T. Adams, P. Addesso, R. X. Adhikari *et al.*, Observation of Gravitational Waves from a Binary Black Hole Merger, Phys. Rev. Lett. **116**, 061102 (2016).

[2] Markus Aspelmeyer, Tobias J. Kippenberg, and Florian Marquardt, Cavity optomechanics, Rev. Mod. Phys. **86**, 1391 (2014).

[3] Stefano Mancini, Vittorio Giovannetti, David Vitali, and Paolo Tombesi, Entangling Macroscopic Oscillators Exploiting Radiation Pressure, Phys. Rev. Lett. **88**, 120401 (2002).

[4] Alexander G. Krause, Martin Winger, Tim D. Blasius, Qiang Lin, and Oskar Painter, A high-resolution microchip optomechanical accelerometer, Nat. Photon. **6**, 768 (2012).

[5] Fenfei Liu, Seyedhamidreza Alaie, Zayd C. Leseman, and Mani Hossein-Zadeh, Sub-pg mass sensing and measurement with an optomechanical oscillator, Opt. Express **21**, 19555 (2013).

[6] Yoshihiro Akahane, Takashi Asano, Bong-Shik Song, and Susumu Noda, High-q photonic nanocavity in a two-dimensional photonic crystal, Nature **425**, 944 (2003).

[7] Emanuel Gavartin, Rémy Braive, Isabelle Sagnes, Olivier Arcizet, Alexios Beveratos, Tobias J Kippenberg, and Isabelle Robert-Philip, Optomechanical Coupling in a Two-Dimensional Photonic Crystal Defect Cavity, Phys. Rev. Lett. **106**, 203902 (2011).

[8] Matt Eichenfield, Ryan Camacho, Jasper Chan, Kerry J Vahala, and Oskar Painter, A picogram-and nanometre-scale photonic-crystal optomechanical cavity, Nature **459**, 550 (2009).

[9] O. Levy, B. Z. Steinberg, M. Nathan, and A. Boag, Ultrasensitive displacement sensing using photonic crystal waveguides, Appl. Phys. Lett. **86**, 104102 (2005).

[10] Zhenfeng Xu, Liangcai Cao, Claire Gu, Qingsheng He, and Guofan Jin, Micro displacement sensor based on line-defect

resonant cavity in photonic crystal, Opt. Express **14**, 298 (2006).

[11] Chengkuo Lee, Jayaraj Thillaigovindan, Chii-Chang Chen, Xian Tong Chen, Ya-Ting Chao, Shaohua Tao, Wenfeng Xiang, Aibin Yu, Hanhua Feng, and G. Q. Lo, Si nanophotonics-based cantilever sensor, Appl. Phys. Lett. **93**, 113113 (2008).

[12] Wonjoo Suh, M. F. Yanik, Olav Solgaard, and Shanhui Fan, Displacement-sensitive photonic crystal structures based on guided resonance in photonic crystal slabs, Appl. Phys. Lett. **82**, 1999 (2003).

[13] Masaya Notomi, Hideaki Taniyama, Satoshi Mitsugi, and Eiichi Kuramochi, Optomechanical Wavelength and Energy Conversion in High-q Double-Layer Cavities of Photonic Crystal Slabs, Phys. Rev. Lett. **97**, 023903 (2006).

[14] Tsan-Wen Lu and Po-Tsung Lee, Ultra-high sensitivity optical stress sensor based on double-layered photonic crystal microcavity, Opt. Express **17**, 1518 (2009).

[15] Young-Geun Roh, Takasumi Tanabe, Akihiko Shinya, Hideaki Taniyama, Eiichi Kuramochi, Shinji Matsuo, Tomonari Sato, and Masaya Notomi, Strong optomechanical interaction in a bilayer photonic crystal, Phys. Rev. B **81**, 121101 (2010).

[16] Leondardo Midolo, P. J. van Veldhoven, M. A. Dundar, R. Notzel, and Andrea Fiore, Electromechanical wavelength tuning of double-membrane photonic crystal cavities, Appl. Phys. Lett. **98**, 211120 (2011).

[17] L. Midolo, F. Pagliano, T. B. Hoang, T. Xia, F. W. M. van Otten, L. H. Li, E. H. Linfield, M. Lermer, S. Höfling, and A. Fiore, Spontaneous emission control of single quantum dots by electromechanical tuning of a photonic crystal cavity, Appl. Phys. Lett. **101**, 091106 (2012).

[18] M. Petruzzella, T. Xia, F. Pagliano, S. Birindelli, L. Midolo, Z. Zobenica, L. H. Li, E. H. Linfield, and A. Fiore, Fully tuneable, purcell-enhanced solid-state quantum emitters, Appl. Phys. Lett. **107**, 141109 (2015).

[19] H. A. Haus, W.-P. Huang, S. Kawakami, and N. A. Whitaker, Coupled-mode theory of optical waveguides, J. Lightwave Technol. **5**, 16 (1987).

[20] N. Caselli, Francesca Intonti, Francesco Riboli, Anna Vinattieri, D. Gerace, L. Balet, L. H. Li, Marco Francardi, Annamaria Gerardino, Andrea Fiore *et al.*, Antibonding ground state in photonic crystal molecules, Phys. Rev. B **86**, 035133 (2012).

[21] F. S.-S. Chien, J. B. Tu, W.-F. Hsieh, and S.-C. Cheng, Tight-binding theory for coupled photonic crystal waveguides, Phys. Rev. B **75**, 125113 (2007).

[22] Eiji Iwase, Pui-Chuen Hui, David Woolf, Alejandro W Rodriguez, Steven G. Johnson, Federico Capasso, and Marko Lončar, Control of buckling in large micromembranes using engineered support structures, J. Micromech. Microeng. **22**, 065028 (2012).

[23] Leonardo Midolo and Andrea Fiore, Design and optical properties of electromechanical double-membrane photonic crystal cavities, IEEE J. Quantum Electron. **50**, 404 (2014).

[24] Raoul Stöckle, Christian Fokas, Volker Deckert, Renato Zenobi, Beate Sick, Bert Hecht, and Urs P. Wild, High-quality near-field optical probes by tube etching, Appl. Phys. Lett. **75**, 160 (1999).

[25] Hans-Jürgen Butt, Brunero Cappella, and Michael Kappl, Force measurements with the atomic force microscope: Technique, interpretation and applications, Surf. Sci. Rep. **59**, 1 (2005).

[26] Ian W. Frank, Parag B. Deotare, Murray W. McCutcheon, and Marko Lončar, Programmable photonic crystal nanobeam cavities, Opt. Express **18**, 8705 (2010).

[27] R. Perahia, J. D. Cohen, S. Meenehan, T. P. Mayer Alegre, and O. Painter, Electrostatically tunable optomechanical "zipper" cavity laser, Appl. Phys. Lett. **97**, 191112 (2010).

[28] Francesca Intonti, Francesco Riboli, N. Caselli, M. Abbarchi, Silvia Vignolini, D. S. Wiersma, Anna Vinattieri, D. Gerace, L. Balet, L. H. Li *et al.*, Young's Type Interference for Probing the Mode Symmetry in Photonic Structures, Phys. Rev. Lett. **106**, 143901 (2011).

[29] A. Femius Koenderink, Maria Kafesaki, Ben C. Buchler, and Vahid Sandoghdar, Controlling the Resonance of a Photonic Crystal Microcavity by a Near-Field Probe, Phys. Rev. Lett. **95**, 153904 (2005).

[30] Francesca Intonti, Silvia Vignolini, Francesco Riboli, Anna Vinattieri, Diederik S. Wiersma, Marcello Colocci, Laurent Balet, Christelle Monat, Carl Zinoni, Lianhe H. Li *et al.*, Spectral tuning and near-field imaging of photonic crystal microcavities, Phys. Rev. B **78**, 041401 (2008).

[31] Benoit Cluzell, Loïc Lalouat, Philippe Velha, Emmanuel Picard, David Peyrade, Jean-Claude Rodier, Thomas Charvolin, Philippe Lalanne, FrÚdÚrique de Fornel, and Emmanuel Hadji, A near-field actuated optical nanocavity, Opt. Express **16**, 279 (2008).

[32] D. A. Lapshin, V. S. Letokhov, G. T. Shubeita, S. K. Sekatskii, and G. Dietler, Direct measurement of the absolute value of the interaction force between the fiber probe and the sample in a scanning near-field optical microscope, Appl. Phys. Lett. **81**, 1503 (2002).

[33] Niccolò Caselli, Francesca Intonti, Federico La China, Francesco Riboli, Annamaria Gerardino, Wei Bao, Alexander Weber Bargioni, Lianhe Li, Edmund H. Linfield, Francesco Pagliano *et al.*, Ultra-subwavelength phase-sensitive fano-imaging of localized photonic modes, Light: Sci. Appl. **4**, e326 (2015).